CrystEngComm

PAPER

View Article Online
View Journal | View Issue

Cite this: *CrystEngComm*, 2016, **18**, 6594

Amorphous and crystalline calcium carbonate phases during carbonation of nanolimes: implications in heritage conservation†

Carlos Rodriguez-Navarro,*[a] Kerstin Elert[a] and Radek Ševčík[b]

Received 24th May 2016,
Accepted 13th July 2016

DOI: 10.1039/c6ce01202g

www.rsc.org/crystengcomm

Nanolimes are alcohol dispersions of colloidal $Ca(OH)_2$ nanoparticles used as novel nanomaterials for the conservation of cultural heritage. Upon exposure to atmospheric CO_2 at room *T*, and in the presence of H_2O, they undergo carbonation forming $CaCO_3$ cement which consolidates decayed porous materials such as stone or mural paintings. Despite extensive research on the synthesis and applications of nanolimes, little is known about the mechanisms and kinetics of the formation and transformation of metastable and stable calcium carbonate phases and their effects on the treatment efficacy. This is a strong handicap to their effective and widespread application. Here we show that the carbonation of nanolimes in humid air at room *T* involves the initial formation of amorphous calcium carbonate (ACC) and its transformation into metastable vaterite (and minor aragonite) *via* a dissolution–precipitation process, followed by non-classical nanoparticle-mediated crystal growth. Subsequently, vaterite (and aragonite) partially dissolves and stable calcite precipitates. All these phase transformations follow first order kinetics, where the rate controlling step is the amount of undissolved parent phase. We unambiguously demonstrate that precipitation of vaterite (up to ~35 wt%) and aragonite (~5 wt%) after ACC (up to ~24 wt%) is favored by the alcohol adsorbed on $Ca(OH)_2$ nanoparticles undergoing carbonation. Although it is known that vaterite formation limits consolidation, the fast kinetics of the solvent-mediated vaterite–calcite transformation (72% conversion in ten days) ensures that, in the short-term, the almost full consolidation potential of nanolimes can be achieved. Finally, the mechanistic and kinetic commonalities between nanolime carbonation and biomineralization/biomimetic synthesis of $CaCO_3$ underline that the observed multistep crystallization and non-classical crystal growth might be general and applicable for the rational design of novel $CaCO_3$ materials.

1. Introduction

The built and sculptural heritage is subjected to a range of weathering processes (*e.g.* salt weathering, freeze–thawing, air pollution, and biodeterioration) that endanger its survival.[1] Traditional protection/consolidation treatments applied to halt or minimize the deleterious effects of such weathering phenomena included organic polymers (*e.g.* acrylic and epoxy resins), alkoxysilanes (*e.g.* ethyl silicate), and inorganic materials (*e.g.* alkali silicates, $Ba(OH)_2$, ammonium phosphates, and limewater).[1–4] In many cases, however, such "traditional" conservation materials either had limited efficacy or exacerbated damage.[2] This has prompted the development of novel, more efficient nanotechnologies for the cleaning, deacidification, protection and consolidation of ornamental materials.[3] Among them are alcohol dispersions of colloidal $Ca(OH)_2$ nanoparticles (~30–300 nm in size), the so-called nanolimes.[2–4] When applied on weathered porous materials such as stone, mortars or mural paintings, they rapidly penetrate into the porous system of the treated substrate and, in contact with atmospheric CO_2 and in the presence of humidity, undergo carbonation. Carbonation is commonly represented by the following overall reaction: $Ca(OH)_2 + CO_2 = CaCO_3 + H_2O$. However, carbonation involves several steps: (i) dissolution of $Ca(OH)_2$ in adsorbed and/or pore water, releasing Ca^{2+} and OH^- ions, (ii) dissolution of gaseous CO_2 in this alkaline solution (pH ~ 12.4) as a loosely hydrated aqueous form, which at such a high pH reacts with OH^- ions forming bicarbonate (HCO_3^-) ions that rapidly dissociate forming carbonate (CO_3^{2-}) ions (at lower pH values, CO_2 hydration results in H_2CO_3 which subsequently dissociates into HCO^{3-} and CO_3^{2-}), and finally, (iii) reaction between Ca^{2+} and CO_3^{2-} ions forming calcium carbonate.[5,6] The newly formed $CaCO_3$

[a] *Dept. of Mineralogy and Petrology, University of Granada, Fuentenueva s/n, 18002 Granada, Spain. E-mail: carlosrn@ugr.es*
[b] *Institute of Theoretical and Applied Mechanics AS CR, Centre of Excellence Telč, Batelovská 485-486, 588 56 Telč, Czech Republic*

† Electronic supplementary information (ESI) available: Additional figures (Fig. S1–S6), including XRD, FTIR, Raman, TG/DSC results, and FESEM photomicrographs. See DOI: 10.1039/c6ce01202g

cement binds loose grains and/or fills cracks, consolidating and strengthening the decayed porous material.[3,7] Nanolime-based consolidation is particularly effective in the case of carbonate-based materials (*e.g.* limestone or marble), due to the high compatibility between the newly-formed cement and the substrate which share the same composition and structure.[8,9] Because the nanoparticles are applied as colloidal alcohol dispersions, no water is introduced into the porous system of the treated material, hence preventing any deleterious effects associated with this latter solvent (*e.g.* dissolution and/or freeze damage).[3] Furthermore, the amount of $Ca(OH)_2$ in nanolime dispersions can be orders of magnitude higher than that dissolved in traditional "limewater" treatments (which is limited by the solubility of $Ca(OH)_2$, ~1.8 g L^{-1} at 20 °C).[2,4] This enables the formation of sufficient amounts of $CaCO_3$ cement so as to achieve a high level of consolidation.[3]

Despite the numerous studies on the synthesis and application of nanolimes for the conservation of cultural heritage (see ref. 3 for a recent review), little is known about the kinetics and mechanisms of their carbonation. The latter strongly influences their consolidation effectiveness. Depending on the environmental conditions, particularly relative humidity (RH), the carbonation rate of $Ca(OH)_2$ nanoparticles and final yield (*i.e.* fractional conversion of $Ca(OH)_2$ into $CaCO_3$), as well as the resulting $CaCO_3$ phase(s), can vary significantly[7–9] and so does their effectiveness.[7] There is, however, no consensus regarding what phases form at a particular RH and what is the phase evolution over time. The formation of metastable $CaCO_3$ precursor phases, including amorphous calcium carbonate (ACC), monohydrocalcite, vaterite and aragonite, prior to or along with stable calcite has been reported.[7,9–12] Such phases and precipitation sequence are not exclusive of nanolime carbonation: they have also been observed during the setting and hardening of lime mortars,[6] the precipitation of carbonates in aqueous solutions,[13] and in biomineralization and biomimetic precipitation of $CaCO_3$ structures.[14] It is, however, not fully clear what determines the formation of a particular calcium carbonate phase or a particular (multistep) crystallization sequence, although kinetics appear to be a key factor.[6,14] It is also not well known whether the transformation from one phase to another occurs through nucleation of the more stable phase within the existing precursor or through dissolution of the parent phase and reprecipitation of the secondary phase.[15]

The kinetics and mechanisms of $Ca(OH)_2$ carbonation in solution (aqueous phase or aqueous dispersion) have been extensively studied due to the relevance of this process in the synthesis of precipitated calcium carbonate (PCC) for industrial applications (*e.g.* plastics, drugs, paper, rubber, paints).[16–20] Typically, carbonation of $Ca(OH)_2$ slurries *via* injection of CO_2 involves the formation of metastable precursor phases both amorphous and crystalline (vaterite and aragonite) and their partial or complete transformation into stable calcite.[16–18] A very similar precipitation sequence has been observed during the thoroughly studied homogeneous precipitation of $CaCO_3$ in solution.[13,15,21–23] In both cases, the main parameters controlling the kinetics of $CaCO_3$ formation and solid phase evolution/polymorph selection are supersaturation, pH, T, $[Ca^{2+}]/[CO_3^{2-}]$, pCO_2, and (organic or inorganic) additives. In contrast, little research has been dedicated to understand the kinetics and mechanisms of $Ca(OH)_2$ carbonation in air at room T, conditions that are relevant during the application of nanolimes in cultural heritage conservation,[9] as well as during the setting and hardening of traditional lime mortars.[6,24,25] Experimental results showed that the main parameters that affect the carbonation rate and polymorph selection during such a gas–solid reaction are RH, T, reactant surface area, and pCO_2, in addition to impurities/additives (*e.g.* Mg ions and organic additives).[19,24,26–28] A consensus on the crucial role of humidity in determining the rates of $Ca(OH)_2$ carbonation in air at low T exists.[10,26–29] Shih *et al.*[26] reported that carbonation rates are nearly zero at RH $<$ 8% and undergo a sigmoidal-type increase with increasing RH. This is consistent with AFM observations of the carbonation of portlandite crystals showing that newly formed surface precipitates (*i.e.* $CaCO_3$) only occurred at RH $\geq$ 30%.[29] Beruto and Botter[27] pointed out that the formation of an adsorbed (liquid-like) water film on $Ca(OH)_2$ particles was critical for carbonation to progress and indicated that at RH $>$ 70% carbonation rates increase exponentially due to multilayer water adsorption. The authors concluded that adsorbed liquid-like water played a catalytic role in this gas–solid reaction, which actually was considered a gas–liquid–solid reaction. Dheilly *et al.*[28] indicated that at a sufficiently high RH ($>>$30%) CO_2 and $Ca(OH)_2$ dissolved in the adsorbed water film, and finally, $CaCO_3$ precipitated onto portlandite. The product H_2O could autocatalyze the carbonation reaction until completion or until a passivating product ($CaCO_3$) layer would prevent the advancement of the reaction front to the core of portlandite particles.[19,25] However, no consensus has been reached regarding the kinetic and mechanistic models that best describe $Ca(OH)_2$ carbonation in air at low T. Whereas some researchers found that carbonation is a deceleratory process displaying no induction time,[18,19,26,28] others indicated that it follows sigmoidal-type Avrami–Erofeev kinetics with an induction time before nucleation and growth.[9] The disagreement in the proposed kinetic (and mechanistic) models may lie in the fact that previous studies did not consider the possible role of metastable precursor phases (ACC and vaterite, in particular) in the carbonation process. Because carbonation kinetics determine the time frame for achieving the intended consolidation effect of nanolimes, a good understanding of the factors that influence the carbonation rate and its mechanism is critical. Furthermore, the formation and kinetic stabilization of precursor phases, such as vaterite, lead to a lower level of consolidation than that achieved following formation of stable calcite.[7] Despite the fact that in solution vaterite is readily converted (within hours) into calcite at room T,[13,23,30] the kinetics of this phase transformation have not yet been studied for the case of nanolimes undergoing carbonation in air (*i.e.* vaterite-to-calcite conversion in *in situ* real application).

It is our aim to study the carbonation of a commercial nanolime exposed to humid air at room T in order to disclose the exact crystallization sequence of metastable and stable phases formed upon $Ca(OH)_2$ nanoparticle carbonation and to provide insight into their carbonation mechanism. Ultimately, we strive to show that the kinetics of nanolime carbonation are strongly related to the formation of metastable precursor phases: first, ACC, and later on, vaterite (and aragonite), which is eventually converted into stable calcite following the Ostwald's step rule.[13,14] The implications of our results on the application (and limitations) of nanolimes as new nanomaterials for the conservation of cultural heritage, as well as for the design of novel $CaCO_3$ (biomimetic) materials, are discussed.

2. Experimental section

2.1. Nanolime

A commercial nanolime (CaLoSil® E-25) was purchased from IBZ-Salzchemie (Freiberg, Germany). CaLoSil® E-25 is an ethanol dispersion of colloidal $Ca(OH)_2$ nanoparticles (25 wt% solids content). Nanoparticles are prepared following hydrolysis of a Ca-alkoxide precursor and subsequent dispersion into ethanol.[8]

2.2. Carbonation of nanolime

Alcohol dispersions of $Ca(OH)_2$ nanoparticles (*ca.* 2 mL) were sonicated for 5 min, deposited on glass slides (3 cm in diameter) and subjected to drying in air at room T for 60 min. Once dry, the samples were placed in a plastic container at 18 ± 2 °C and 80 ± 5% RH. The container was not air-tight in order to allow for a small but continuous flux of air ($pCO_2 \sim 10^{-3.5}$ atm) to promote carbonation. A relatively high RH was selected in order to accelerate the carbonation process.[7,27] Samples were collected at predetermined time intervals (up to 21 days), and their degree of $CaCO_3$ transformation as well as the mass fraction of crystalline $CaCO_3$ polymorphs were determined by means of X-ray diffraction (XRD) and thermogravimetry (TG) (see details below). Additionally, we used *in situ* Raman spectroscopy (DXR, Thermo Scientific) to monitor the early stages (0 to 24 h) of nanolime carbonation. Raman spectra were collected in the spectral range of 3500–50 cm^{-1} (each spectrum was collected using 60 × 15 s and 200 × 10 s exposure times for room-dried and oven-dried samples—1 h at 100 °C, see details below, respectively) with the 532 nm laser beam focused with a 10× objective. The baseline correction was performed using the routine implemented in the software Omnic v. 9.1.24.

2.3. Analysis of reactant and product phases

The mineralogy of solids was determined by XRD using a PANanalytical XPert Pro with a Ni filter. The measurement parameters were as follows: Cu Kα radiation λ = 1.5405 Å, 45 kV, 40 mA, 4 to 70° 2θ exploration range, steps of 0.001° 2θ, and goniometer speed of 0.01° 2θ s^{-1}. Powders were deposited on zero-background Si sample holders, whereas glass mounts subjected to carbonation for different periods of time were directly subjected to XRD analysis without further preparation. Mineral phases were identified by comparison with JCPDS powder spectra (Joint Committee on Powder Diffraction Standards). Quantitative phase analysis (QPA) was performed by the Rietveld method,[31] using Topas 4.2 software from Bruker AXS.

TG and differential scanning calorimetry (DSC) analyses were performed simultaneously using a Mettler-Toledo TGA/DSC1 coupled to Fourier transform infrared spectroscopy (FTIR) equipment (ThermoFisher Nicolet IS10) for evolved gas analysis. Samples of ~40 mg were placed in Al crucibles and analyzed in flowing N_2 (50 mL min^{-1}) at a heating rate of 20 °C min^{-1} (25 °C to 950 °C).

Additional compositional and microstructural features of $Ca(OH)_2$ particles and carbonation products were determined by means of (i) transmission electron microscopy (TEM, using either a Titan, 300 kV acceleration voltage, or a Philips CM20, 200 kV). Powder samples were dispersed in ethanol, sonicated for 30 s, and collected using holey Formvar™ C-coated Cu grids. TEM observations were performed using a 30 μm objective aperture. SAED patterns were collected using a 10 μm aperture, which allowed collection of diffraction data from a circular area ~0.2 μm in diameter; (ii) field emission scanning electron microscopy (FESEM, Auriga, Zeiss). Samples were carbon coated prior to analysis; (iii) FTIR (JASCO 6200), frequency range of 400–4000 cm^{-1} and 4 cm^{-1} spectral resolution. This FTIR is equipped with an attenuated total reflectance (ATR) device for spectra collection without sample preparation (*i.e.* to minimize artifacts such as dehydration of ACC); (iv) N_2 sorption (Micromeritics TriStar 3000). The surface area (BET method) of solids was determined by means of N_2 adsorption at 77 K following degassing for 3 h at 80 °C under vacuum using a Micromeritics FlowPrep device; (v) the particle size distribution (PSD) of nanolime ethanol dispersions was determined by laser scattering using Malvern Hydro 2000μp equipment. Further details on sample preparation and specific characteristics of the above-listed analytical equipment have been published elsewhere.[7,20]

3. Results and discussion

3.1. Nanolime characterization

FESEM and TEM observations showed that the nanolime was made up of plate-like hexagonal-shaped portlandite ($Ca(OH)_2$) nanoparticles with length (measured along [110]) ranging from 35 to 235 nm (average ± std. dev.: 134 ± 57 nm) and thickness (measured along [001]) ranging from 15 to 40 nm (25 ± 8 nm) (Fig. 1). In some cases, aggregates of a few (~3–12) particles with a size of ~300–600 nm were observed using TEM.

XRD, FTIR, and TG/DSC analyses confirmed that the nanolime was made up of portlandite crystals with minor amounts of $CaCO_3$ (≤5.2 wt% according to TG analysis) (Fig. S1a–c†). The size of the nanoparticles determined by laser scattering was 34–400 nm (mode = 138 nm) (Fig. S1d†). The BET surface area (obtained from N_2 sorption isotherms; see Fig. S1e†) was

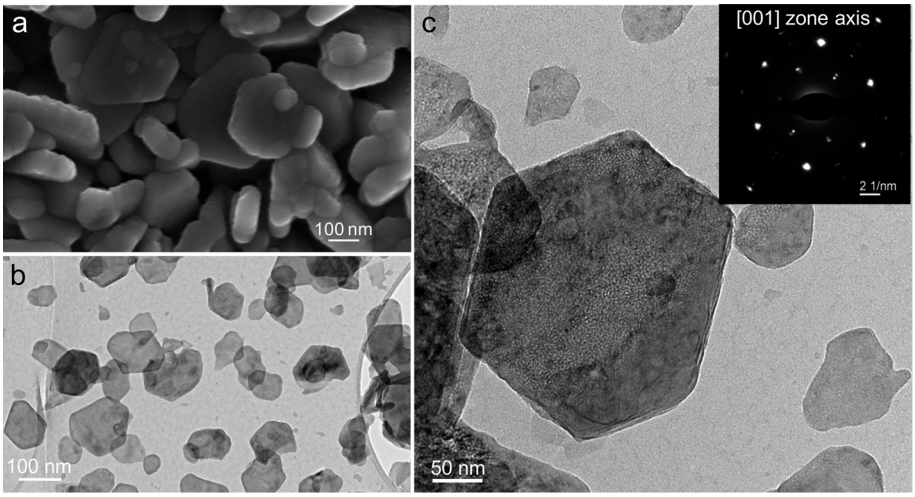

Fig. 1 FESEM and TEM-SAED analysis of nanolime. (a) FESEM photomicrograph and (b) TEM bright field image of portlandite nanoparticles. Note the porous structure formed upon drying of nanolime dispersions deposited on a glass slide (a); (c) TEM details of the hexagonal plate-like $Ca(OH)_2$ nanoparticle (the SAED pattern is shown in the inset).

$31.4 \pm 0.5\ m^2\ g^{-1}$. All these features are standard for commercial nanolimes.[7,9–11]

3.2. The early stage of nanolime carbonation: formation of ACC

XRD analyses showed that no crystalline $CaCO_3$ phase formed during the first 2–4 h of exposure to atmospheric CO_2 (Fig. 2a). However, TG/DSC analyses disclosed that at this point the amount of $CaCO_3$ was up to ~13–24 wt% (Fig. 2b). Furthermore, TG traces displayed a marked weight loss at 100–350 °C, while DSC analyses showed an exothermic peak at ~330 °C. These features are characteristic of the thermal dehydration of ACC followed by its transformation into calcite.[32] To confirm that ACC formed during the early stages of carbonation, nanolime samples exposed to carbonation in humid air for 3 h (*i.e.* showing no Bragg peaks corresponding to crystalline $CaCO_3$ phases) were heated for 30 min in an oven at 350 °C (*i.e.* just above the reported *T* for the complete dehydration of ACC and its conversion into calcite).[32] XRD analysis of heat-treated samples showed the appearance of broad and intense Bragg peaks corresponding to calcite (Fig. 2a). These results demonstrate that ACC is the only carbonate phase formed during the initial stages of nanolime carbonation in humid air.

TEM observations provided further evidence for the formation of ACC (Fig. 3). Interestingly, some hexagonal-shaped portlandite crystals displayed a hollow (dissolved) center in their {0001} basal faces, thereby displaying a ring-like structure (Fig. 3a and b). However, SAED patterns showed that such structures were amorphous (see inset in Fig. 3b). FESEM revealed the presence of nanogranular precipitates covering the surface of the hexagonal plate-like $Ca(OH)_2$ crystals (Fig. S2†), similar to those observed by Yang *et al.*[29] These observations indicate that ACC pseudomorphically replaced portlandite crystals, thereby preserving the overall external shape of the portlandite precursor. The fact that the center of former portlandite plate-like crystals was dissolved suggests that the most likely mechanism for this pseudomorphic replacement is an interface-coupled dissolution–precipitation mechanism.[33]

To corroborate that water was crucial for the formation of ACC, nanolime samples were placed in a container with silica gel (RH ~ 0%) at room *T*. Under such dry conditions, no ACC (or any other calcium carbonate phase) formed even after 2 months storage time, despite the fact that the samples were in contact with atmospheric CO_2. These results demonstrate that water is necessary for the formation of ACC during carbonation of $Ca(OH)_2$ and provide strong evidence (along with TEM observations) that ACC formation after $Ca(OH)_2$ involves multilayer H_2O adsorption onto $Ca(OH)_2$ crystals,[27] followed by a dissolution–precipitation mechanism. Such a process is likely being enhanced by capillary condensation of H_2O into the mesoporous structure (Fig. 1a and S1e†) formed upon deposition and drying of nanolime dispersions (on glass slides), as well as by H_2O release following $Ca(OH)_2$ carbonation.[19] In addition to the above-described ACC pseudomorphs, rounded ACC nanoparticles (40 to 100 nm in size) were observed either isolated or forming aggregates commonly connected by necks. Their amorphous nature was confirmed by the broad and diffuse rings in the SAED patterns (Fig. 3c and d). The lack of spatial connection between these latter ACC nanoparticles and the ACC pseudomorphs suggests that they formed *via* homogeneous nucleation in the above-mentioned aqueous solution film. The formation of ACC indicates that a very high supersaturation was reached during the early stages of carbonation, as we have quantitatively demonstrated for the initial stages of carbonation of saturated $Ca(OH)_2$ solutions exposed to atmospheric CO_2.[20]

3.3. The advanced stages of nanolime carbonation: formation of crystalline $CaCO_3$ polymorphs

XRD analysis showed that after 6 h carbonation time, vaterite and calcite formed along with trace amounts of aragonite

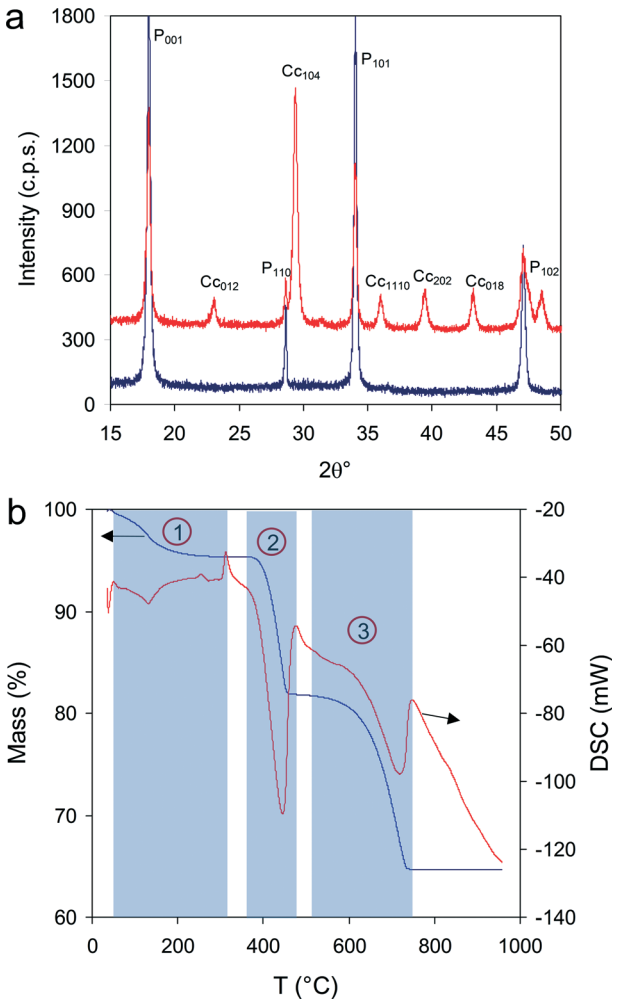

Fig. 2 XRD analysis of nanolime subjected to carbonation for 3 h. a) XRD patterns of portlandite (P) showing no Bragg peaks of crystalline $CaCO_3$ (blue line) and the appearance of calcite (Cc) Bragg peaks following heat-induced transformation of ACC (red line) (see text for details); b) TG/DSC traces showing (shaded areas) dehydration and crystallization of ACC (1), dehydroxylation of $Ca(OH)_2$ (2) and calcination of $CaCO_3$ (3).

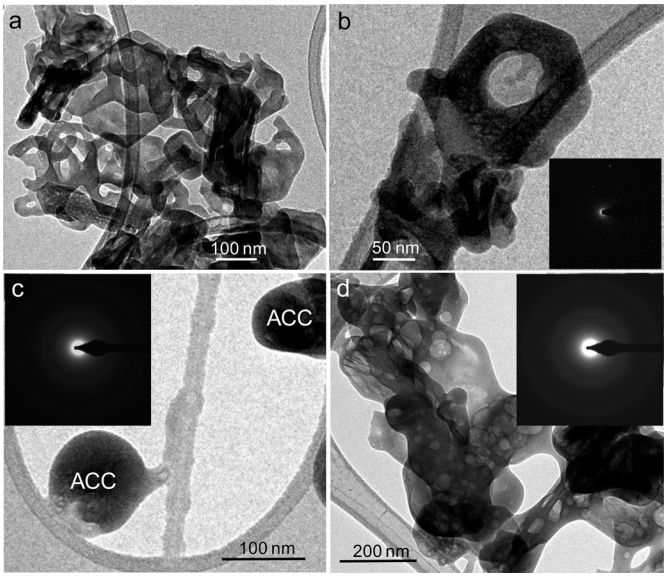

Fig. 3 TEM observations of ACC formed following carbonation of $Ca(OH)_2$. a) Hexagonal-shaped ACC pseudomorphs (after portlandite hexagonal platelets); b) details of the ring-like ACC pseudomorph (the SAED pattern is shown in the inset); c) isolated ACC nanoparticles (the SAED pattern is shown in the inset); d) aggregate of ACC nanoparticles (the SAED pattern is shown in the inset).

(Fig. 4a and S3†). Note that vaterite Bragg peaks at 1 day carbonation time were very broad and slightly shifted (to lower 2θ values) from the position corresponding to the most accepted vaterite structures (see below) (Fig. S3†).[34,35] To properly quantify the vaterite content using Rietveld full profile fitting, two different vaterite structures had to be used: that of Meyer[35] ($P6_3mc$) and that of Demichelis *et al.*[36] ($C2$).[37] This is consistent with recent computer simulations[36] and experimental findings[38] showing that vaterite can display multiple structures that are commonly interspersed.

The amount of vaterite increased rapidly during the first 24 h carbonation time but decreased afterwards. Concomitantly, the $Ca(OH)_2$ content decreased while that of calcite continuously increased. In parallel, the aragonite content increased up to 1 day and afterwards decreased. Fig. 4b shows the TG results for the *t*-dependent phase evolution. In this latter case, portlandite, ACC, and total anhydrous crystalline $CaCO_3$ phases (calcite + vaterite + aragonite) were quantified.

We determined the total $CaCO_3$ content by measuring the weight loss at 550–800 °C associated with the decomposition of $CaCO_3$ into CaO + CO_2. The ACC content was calculated from the H_2O loss (due to ACC dehydration) at 120–350 °C, assuming the following structural formula: $CaCO_3{\cdot}1.5H_2O$. Note that a water content of ~1.4–1.5 mol per formula unit is typical for ACC formed following carbonation (at high pH) of $Ca(OH)_2$ saturated solutions.[20] From the total $CaCO_3$ content, the fractional amount of ACC was subtracted, with the remaining fraction being crystalline $CaCO_3$. Fig. 4b shows that the ACC content continuously decreased after the first hours of carbonation. Despite its well-known instability, minor amounts of ACC were still present after 2–5 days carbonation (*i.e.* as long as there was a reservoir of uncarbonated $Ca(OH)_2$). At longer carbonation times, however, the calculated ACC content was negligible (almost zero, within error).

These results show that irrespective of the fractional amount of carbonated $Ca(OH)_2$, carbonation systematically involved the initial formation of ACC, followed by its transformation into crystalline $CaCO_3$ phases. They also show that immediately after ACC, vaterite (as well as aragonite) formed along with calcite. However, the fact that the vaterite (and aragonite) content rapidly decreased concurrently with a continuous increase in the calcite content shows that vaterite (and aragonite) transformed into stable calcite. The possibility of a direct vaterite-to-aragonite transformation is ruled out, because both phases displayed a continuous and parallel decrease in their fractional content. These observations are consistent with recent studies showing that (i) both vaterite

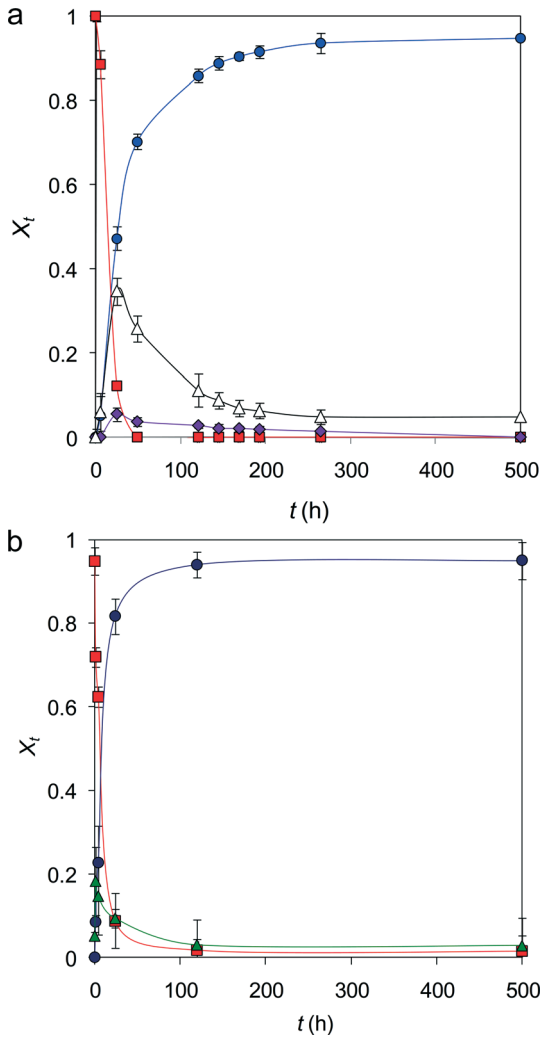

Fig. 4 Time evolution of the fractional amount (X_t) of calcium carbonate phases during nanolime carbonation. a) XRD results and b) TG results (see text for details). Symbols: $Ca(OH)_2$, ■; calcite, ●; vaterite, Δ; aragonite, ◆; crystalline $CaCO_3$, ●; ACC, ▲.

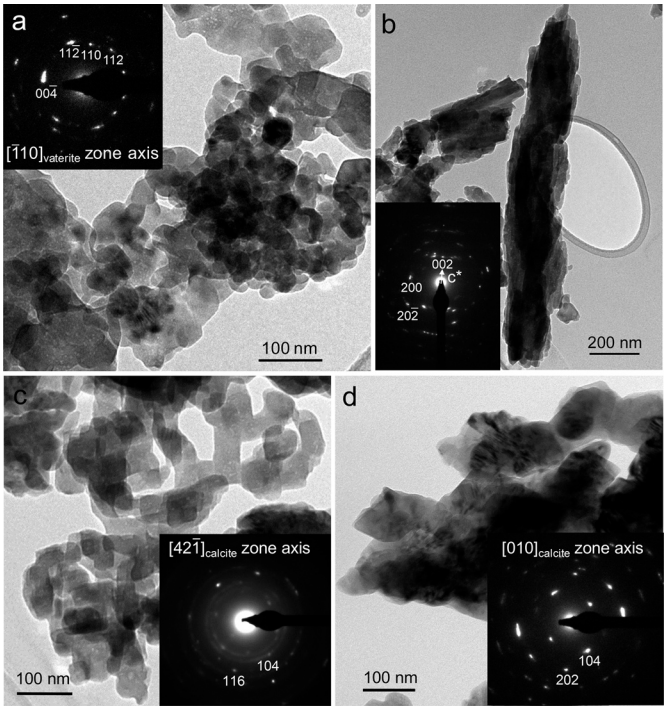

Fig. 5 TEM images of $CaCO_3$ polymorphs formed during nanolime carbonation. a) Porous vaterite structure made up of oriented nanoparticles (the SAED pattern is shown in the inset) and b) aragonite spindle-like structures made up of oriented nanorods. The SAED pattern (inset) corresponding to the larger (vertical) structure shows multiple, superposed reflections corresponding to [010] and [$\bar{1}$10] zone axis patterns (due to twinning along {110}). The orientation of the c^* (reciprocal) axis is indicated; c) the calcite structure made up of an aggregate of oriented nanoparticles. The SAED pattern (inset) shows extra Debye rings due to CaO formation after e-beam induced decomposition of $CaCO_3$ (such nanocrystals were highly sensitive to beam damage); d) more evolved calcite aggregate displaying arced diffraction spots (the SAED pattern is shown in the inset) due to slight misorientation among constituent calcite nanocrystals.

and aragonite form after dissolution of ACC,[15] (ii) they can grow simultaneously and independently after ACC,[39] and (iii) in additive-free systems their dissolution systematically results in the formation of calcite.[15,39–41]

TEM imaging showed nearly-rounded and porous vaterite structures (~200–600 nm in size) made up of an aggregate of nanoparticles 15–30 nm in size (Fig. 5a). The very small size of individual nanoparticles may help explain the broadness of vaterite Bragg peaks, especially those corresponding to 24 h carbonation time that overlapped those of aragonite in the 25–30° 2θ range (Fig. S3†). Vaterite structures diffracted electrons as a single crystal but with an angular spreading in SAED spots of ~10–15° (see inset in Fig. 5a). All these features are common to many synthetic vaterite structures[40,42] and are also characteristic of mesocrystals.[14,43,44] They suggest that vaterite formed *via* aggregation of colloidal nanoparticles. This non-classical particle-mediated crystal growth mechanism seems to be general for the formation of vaterite superstructures,[45,46] as well as several $CaCO_3$ biominerals and their biomimetics.[14,47] Note, however, that the formation of vaterite structures (typically of nearly spherical shape) has been a matter of controversy. Another theory suggests that they do not form *via* nanoparticle aggregation but rather *via* classical spherulitic growth (see below).[48]

Additionally, a few elongated aragonite structures (up to 1.6 μm in length) with a spindle-like morphology (Fig. 5b) and abundant aggregates of calcite rhombohedra (Fig. 5c and d) were observed (using TEM) after 6 h carbonation time. The former were made up of an aggregate of oriented aragonite nanorods with a length of ~100–200 nm and a thickness of ~20–40 nm (Fig. 5b). Such a type of self-organized aragonite mesostructures has been previously described.[41,49] Zhou *et al.*[49] suggested that the driving force for self-assembly may originate from the inherent anisotropic dipole–dipole interactions between aragonite nanorods.

The observed submicrometer-sized rhombohedral structures (80 nm up to 200 nm) were made up of smaller individual nanometer-sized calcite rhombohedra (30 to 50 nm in size) aggregated in an oriented fashion as shown by TEM-SAED (Fig. 5c and d). Such calcite structures diffracted as a

single crystal with a relatively high angular spreading of up to ~12° in diffraction spots (see inset in Fig. 5d). As stated above for the case of vaterite, these structural features are commonly found in $CaCO_3$ mesocrystals and suggest that these calcite structures formed by oriented aggregation of calcite nanoparticles.[44] Similar mesostructural features have been identified in calcite biominerals such as sea-urchin spines,[50,51] as well as in biomimetic calcite.[44] Note, however, that unlike in biominerals or biomimetic calcite, in our system no (bio)macromolecules or polymeric additives, which are considered critical for the development of mesocrystals,[14] were present. Note also that it has been recently indicated that some mesostructural features observed in assumed $CaCO_3$ mesocrystals can be misleading.[52] Hence, our results do not enable us to conclude that we have obtained genuine calcite (or vaterite) mesocrystals.

Interestingly, FESEM observations showed that the surface of some calcite crystals (recognized by their rhombohedral shape) was partially covered by an aggregate of rounded nanoparticles 30–60 nm in size (Fig. S4†). Their strong resemblance to ACC nanoparticles suggests that these calcite crystals could grow *via* direct attachment of ACC nanoparticles. This is a non-classical calcite crystal growth mechanism that has been recently demonstrated using *in situ* AFM in combination with *ex situ* HRTEM.[53]

After 24 h and up to 21 days carbonation time, no significant textural or compositional changes were observed using TEM and FESEM other than (a) the abundance of ACC was drastically reduced over time, and no ACC nanoparticles remained after 21 days carbonation time; (b) in parallel, the amount of vaterite structures was also drastically reduced, although a few aggregates similar to those detected at the earlier stages of carbonation (24 h) were observed (Fig. 6); (c) the amount of calcite increased and euhedral rhombohedra (up to 400 nm) with no angular spreading in diffraction spots appeared (Fig. 7); (d) larger (up to ~2 μm long and ~50 nm thick) but scarce aragonite prisms were present (Fig. 8). The latter displayed complex SAED patterns due to twinning along {110} (see inset in Fig. 8b). It is most likely that both calcite and aragonite coarsened *via* an Ostwald ripening process.

Overall, these results show that carbonation of nanolime at high RH and low *T* follows the Ostwald's step rule, represented here by the sequence ACC → vaterite → aragonite → calcite (*i.e.* from the less stable, more soluble phase, to the most stable, less soluble phase). This is in agreement with our previous results for the carbonation of lime mortars,[6] as well as for the phase evolution during the carbonation of $Ca(OH)_2$ saturated solutions.[20] Note that the above sequence should not be considered as the actual time sequence for phase formation and evolution. For instance, aragonite does not need to form after vaterite but rather after ACC.[15] Similarly, it is possible that locally calcite formed earlier than vaterite or aragonite *via* direct nucleation from solution, growing *via* classical ion-by-ion incorporation and/or *via* non-classical particle-mediated growth.[47] In other areas, in contrast, it could form after dissolution of vaterite (or aragonite), as recently shown using *in situ* fluid-cell TEM.[15]

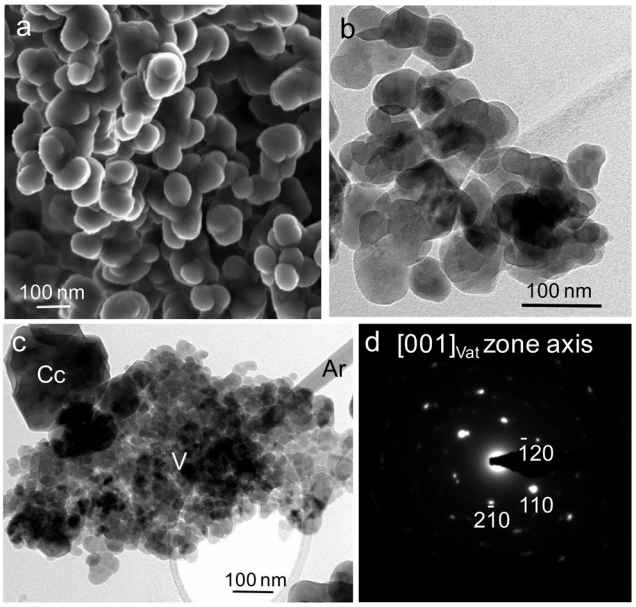

Fig. 6 Vaterite structures after 21 days carbonation time. FESEM (a) and TEM (b and c) photomicrographs of vaterite structures formed by an aggregate of nanoparticles. The SAED pattern of the aggregate in (c) shows that the nanoparticles diffract as a single crystal with a few degrees (~12°) angular spreading (d). Legend: V, vaterite, Cc, calcite, Ar, aragonite.

The fact that all three $CaCO_3$ polymorphs were present from the early stages of carbonation suggests that both direct

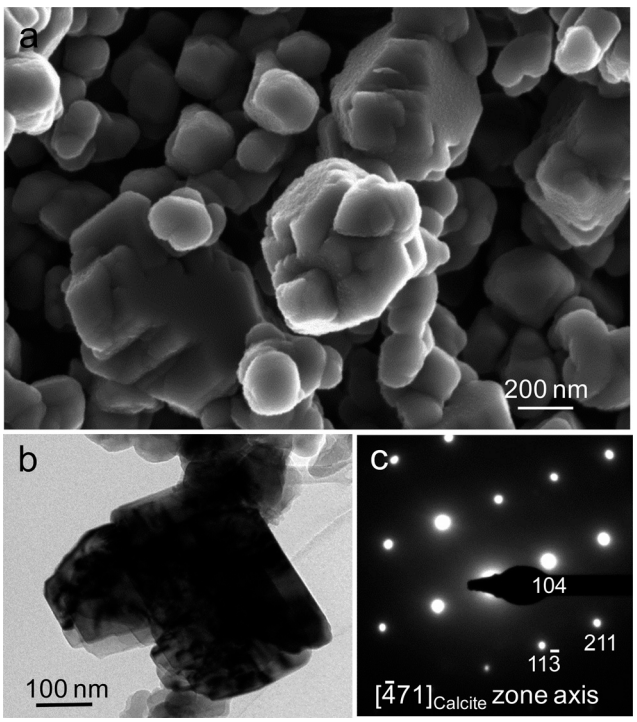

Fig. 7 Calcite crystals after 21 days carbonation time. FESEM (a) and TEM (b) photomicrographs of well developed calcite crystals. The SAED pattern of the calcite rhombohedron in (b) is shown in (c).

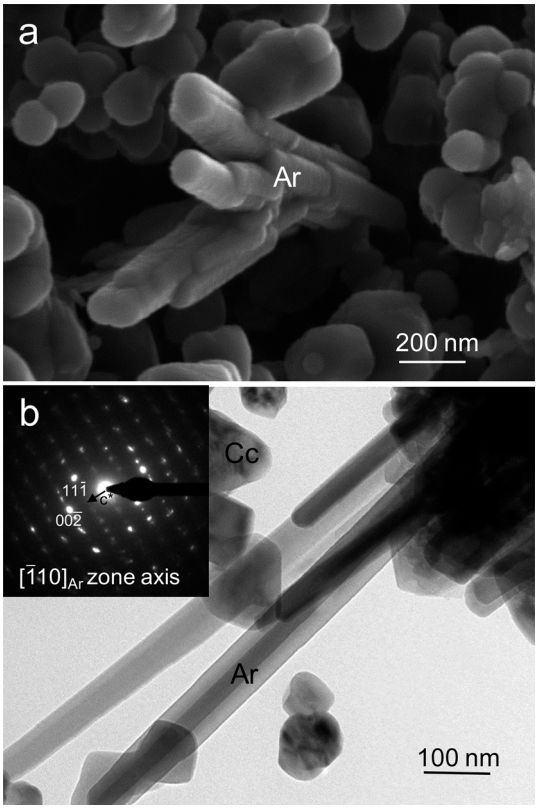

Fig. 8 Aragonite crystals after 21 days carbonation time. FESEM (a) and TEM (b) photomicrographs of well developed aragonite prismatic crystals. The SAED pattern (inset) shows that the crystals grow along [001] and include twinning along {110} which is responsible for the extra spots. The arcing of higher order diffraction spots is related to the slight misorientation of the different prisms making the aggregate depicted in the bright field TEM image. Legend: Cc, calcite; Ar, aragonite.

and indirect crystallization pathways operate in our system.[15] Nielsen *et al.*[15] have shown that vaterite and aragonite can form *via* an indirect pathway after ACC, which is observed to dissolve once these phases nucleate on its surface and grow. In contrast, calcite tends to precipitate either directly from solution or in contact with crystalline precursors (vaterite or aragonite)[23,39,41] but not in contact with ACC.[15] In our case, the most likely mechanistic explanation for the observed crystallization sequence involving ACC-to-vaterite and vaterite-to-calcite transformations (or ACC-to-aragonite and aragonite-to-calcite transformations, yet the trace amounts of aragonite make these pathways less obvious or relevant for the performance of nanolimes) is a kinetically controlled dissolution–reprecipitation process. Note, however, that while consensus on the mechanism of vaterite-to-calcite (or aragonite-to-calcite) transformation exists, which is recognized as a dissolution–reprecipitation process,[13,23,41,54,55] no consensus on the actual mechanism for the transformation of ACC into vaterite and the subsequent formation of mesostructured vaterite exists (the same applies for the case of aragonite). The following mechanisms have been proposed: (i) a solid-state process involving the dehydration and restructuring of ACC nanoparticles to form vaterite nanoparticles that aggregate;[23] (ii) dissolution of ACC and homogeneous precipitation of vaterite nanoparticles that subsequently aggregate into micrometer sized spheres[40] and (iii) vaterite formation *via* ACC dissolution coupled with classical spherulitic growth.[39,48] Recently, however, it has been shown that vaterite nanocrystals can form following heterogeneous nucleation onto (or in) ACC nanoparticles that subsequently dissolve as the (numerous) vaterite nanoparticles surrounding each ACC nanoparticle grow.[15]

Due to the disparate models proposed for the ACC-to-vaterite transformation, we wanted to gain insight into this transformation mechanism in the case of the nanolime tested here. For this task, nanolime samples exposed to atmospheric CO_2 for 3 h, therefore only including ACC and untransformed $Ca(OH)_2$ (see above), were stored in a closed container with silica gel at room *T*. After more than 2 months storage, ACC did not experience any transformation into crystalline $CaCO_3$. This shows that in our experiments the transformation of ACC into crystalline $CaCO_3$ is not a solid-state mechanism and has to involve a water-mediated (dissolution–precipitation) mechanism.

The fact that individual vaterite nanoparticles displayed a rounded morphology and a size typically smaller than that of the ACC precursor is difficult to explain by a process involving the complete dissolution of ACC nanoparticles and the subsequent homogeneous precipitation of vaterite. Due to the limited solubility difference between ACC and vaterite, dissolution of ACC should result in a relatively low saturation index (SI) of 1.4 ($SI = \log(ks_{ACC}/ks_{Vat})$, where ks_{ACC} and ks_{Vat} are the solubility products of ACC and vaterite, respectively).[48] This is not consistent with the observed particle number and size of vaterite nanoparticles that make up the vaterite structures.[48] Indeed, it has been suggested that for the homogeneous nucleation of the nanometer-sized particles typically making up the vaterite structures, a supersaturation several orders of magnitude higher would be required.[48] Considering, however, that several vaterite (nano)crystals can nucleate heterogeneously on an ACC nanoparticle (in equilibrium with an aqueous solution film) and grow at the expense of such an ACC substrate (which dissolves), then several nanoparticles could form with a size similar or even smaller than that of the precursor ACC nanoparticle, without the need for homogeneous nucleation of vaterite (and extreme supersaturation). An *in situ* TEM study by Nielsen *et al.*[15] confirms this sequence of events. Vaterite nanoparticles can later on aggregate in an oriented fashion forming the mesostructures observed here. Besides, the nanostructural features of the vaterite mesostructures observed here (*e.g.* high angular spreading of diffraction spots, high interparticle porosity, absence of well-defined crystal faces in individual nanoparticles, and reduced polydispersity) are not compatible with the spherulitic growth.

3.4. The role of ethanol adsorption on $CaCO_3$ polymorph selection

Carbonation of aqueous solutions of $Ca(OH)_2$ or aqueous dispersions of $Ca(OH)_2$ particles at room *T* typically involves the

formation of ACC, its dissolution, and the subsequent formation of calcite.[6,20] However, the formation of vaterite and/or aragonite as observed here is uncommon. We have previously shown that the formation of vaterite during nanolime carbonation is induced by the presence of alcohol released after hydrolysis of calcium alkoxides formed on $Ca(OH)_2$ particles dispersed in alcohol and stored for long periods of time.[7,56] Nonetheless, our FTIR analysis of the nanolimes studied here (oven-dried samples) revealed no Ca-alkoxide (Fig. S1b†). In contrast, our *in situ* Raman analysis revealed that air-dried nanolime particles subjected to carbonation in humid air displayed some weak absorption bands at 2800–2900 cm^{-1} during the first 24 h (Fig. 9a). These bands, whose amplitude decreased over time, corresponded to CH_2 and CH_3 groups of adsorbed ethanol (*i.e.* the dispersing medium of the nanolime suspension). Such samples displayed both aragonite and vaterite, along with calcite, after 24 h carbonation time (Fig. 9b–d).[57] In contrast, samples oven-dried for 1 h at 100 °C prior to carbonation displayed negligible CH_2 and CH_3 bands in the Raman spectrum and resulted in 100% calcite precipitation (no vaterite or aragonite formation) (Fig. S5†).[57] TG/DSC analysis of these samples subjected to 6 h carbonation showed a marked weight loss at 100–350 °C and an exothermal peak at 320 °C corresponding to the dehydration and crystallization of ACC (~27 wt%) (Fig. S6a†). XRD analysis of the latter samples displayed no crystalline $CaCO_3$ phases (other than negligible amounts of calcite) (Fig. S6b†). However, heating the previous samples to 350 °C for 1 h resulted in the appearance of intense calcite Bragg peaks (Fig. S6a†). As indicated above, this is due to the heat-induced crystallization of ACC into calcite.

Overall, these results suggest that (i) the release of the alcohol adsorbed on portlandite into the aqueous film formed upon H_2O adsorption onto $Ca(OH)_2$ crystals caused the formation of a hydro-alcoholic solution film, (ii) dissolution of both CO_2 and $Ca(OH)_2$ into such a hydro-alcoholic solution

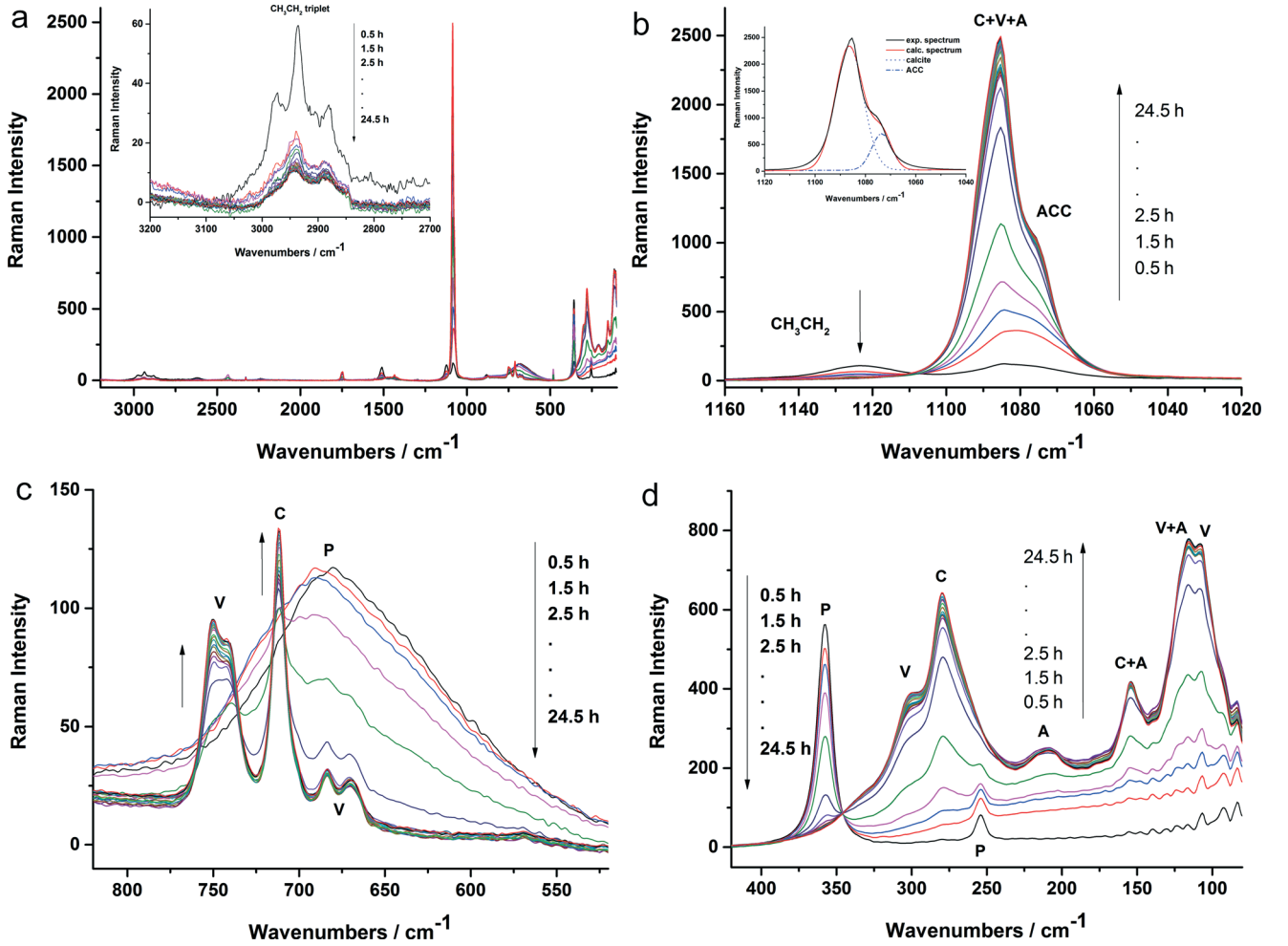

Fig. 9 *In situ* Raman spectroscopy analysis of nanolime carbonation. a) Full Raman spectra of all analyses performed over the first 24 h of the experiment. The inset shows the spectral region corresponding to ethanol; b–d) details of relevant spectral regions showing the formation of different calcium carbonate phases. Deconvolution of the band at ~1080 cm^{-1} (inset in (b)) shows a shoulder that matches the spectral signature of ACC. The bands of portlandite (P) and the characteristic σ_4 bands of the crystalline polymorphs (A: aragonite, V: vaterite and C: calcite) are shown in (c), while the corresponding lattice bands are shown in (d). Assignment of the different bands for calcium carbonate phases was done following ref. 57.

resulted in the initial formation of ACC and, after its dissolution, promoted the formation and kinetic stabilization of vaterite and aragonite during the first 24 h of carbonation. In contrast, heat treatment of nanolime at 100 °C led to the almost complete desorption of ethanol, thereby resulting in calcite formation after ACC following carbonation of $Ca(OH)_2$. Apparently, while ethanol had no significant effect on ACC formation, it had a major effect on the formation of metastable crystalline $CaCO_3$ polymorphs. Fig. 10 schematically shows the crystallization paths, precipitate morphology and phase evolution in our system with and without ethanol.

Alcohols in aqueous solution have been shown to significantly affect the precipitation of calcium carbonate, typically inducing the precipitation and kinetic stabilization of vaterite and aragonite (at room *T*).[41,58–60] Both physical and chemical effects have been proposed to explain $CaCO_3$ polymorph selection and/or stabilization, as well as changes in the morphology of precipitates. The physical effect involves changes in solution viscosity[58] and the incomplete mixing of water and alcohol molecules as well as the divisive effect of alcohol on Ca^{2+} and CO_3^{2-} hydration owing to their different solvation behaviors.[41,60] These effects appear to contribute to changes in the morphology of precipitates.[58,60] The chemical effect relates to changes (increase) in SI.[41,42,61] In addition, face-specific alcohol chemisorption onto metastable $CaCO_3$ phases has been suggested to alter their growth rate and morphology.[41] In our system, polymorph selection does not appear to be associated with differences in the saturation state of the solution with and without ethanol, as in both cases ACC was the precursor for either vaterite + aragonite or calcite (*i.e.* the solubility of ACC marked the upper limit for supersaturation with respect to all three crystalline polymorphs). It could be argued that the main effect of ethanol in our system is related to the kinetic stabilization of metastable vaterite and aragonite. It has been reported that ethanol adsorption onto calcite crystals renders them partially hydrophobic, and as a result, a reduction in their dissolution and growth rates occurs.[62,63] We suggest that adsorption of ethanol onto vaterite and aragonite (formed after ACC) kinetically stabilizes such metastable phases delaying their dissolution-mediated transformation into calcite. We cannot rule out the possibility that ethanol in our system also played a role in the development of the different morphologies and nanostructural features of the different calcium carbonate phases due to the directing role associated with alcohol during vaterite (and aragonite) growth[60] and/or face-specific adsorption.[41]

It is concluded that during real case scenarios (*i.e.* field applications on heritage structures) where nanolimes are subjected to incomplete evaporation/desorption of alcohol adsorbed on $Ca(OH)_2$ nanoparticles, it is likely that abundant metastable $CaCO_3$ polymorphs will form during the early stages of carbonation as observed here.

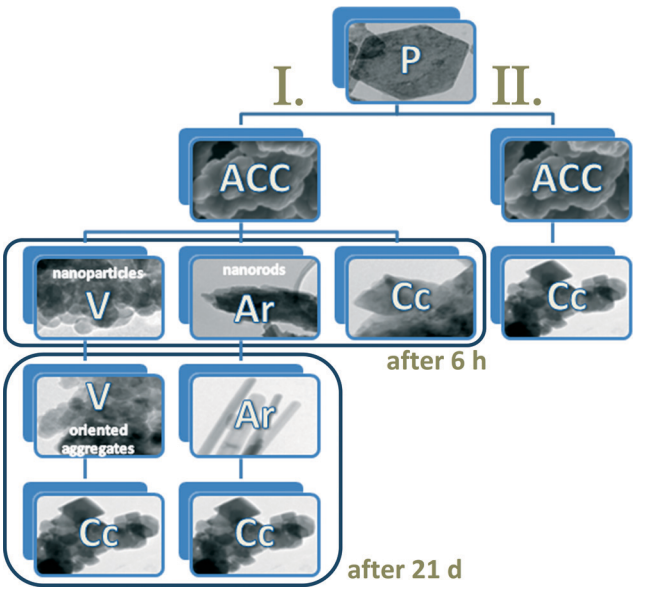

Fig. 10 Crystallization paths in the presence and absence of alcohol. Scheme showing the phase, mesostructure and morphology of precipitates (TEM images) and their temporal evolution in the presence (route I.) and absence (route II.) of adsorbed ethanol. Legend: P, portlandite; V, vaterite; Ar, aragonite; Cc, calcite.

3.5. Kinetics of nanolime carbonation

Fig. 11a shows the time evolution of portlandite and total crystalline $CaCO_3$ (*i.e.* calcite + vaterite + aragonite) content determined from XRD. The kinetics of such a phase transformation can be fitted to an Avrami–Erofeev model.[8] However, our XRD quantification ignores the fact that ACC forms in significant quantities during the early stages of nanolime carbonation in moist air at room *T* (see above). Therefore, such a kinetic model is not realistic. We used TG/DSC to quantify the full amount of $CaCO_3$ (*i.e.* amorphous plus crystalline phases) formed during carbonation (Fig. 4b). TG/DSC results clearly show that nanolime carbonation does not involve any induction time and follows deceleratory (asymptotic) kinetics. We fitted our results to all deceleratory kinetic models listed in Khawan and Flanagan.[64] Poor fittings were obtained for geometrical contraction models (R2 and R3), diffusion models (D1, D2, D3, and D4), and reaction order models (F0, F2 and F3). The best fitting (R^2 = 0.982) was obtained using a first-order (F1) kinetic model, analogous to the pseudo-first order kinetic model previously used to fit the kinetics of gas–solid carbonation of $Ca(OH)_2$ slurries during PCC production.[18,19] The differential form for such a kinetic model is

$$\frac{dX_t}{d_t} = k\left(X_{max} - X_t\right)^n \quad (1)$$

where X_t and X_{max} are the fractional amounts of $Ca(OH)_2$ converted into $CaCO_3$ at time *t* and at maximum conversion, respectively, *k* is the rate constant of $Ca(OH)_2$ carbonation and *n* is the order of the reaction (*n* = 1 for F1). Integration

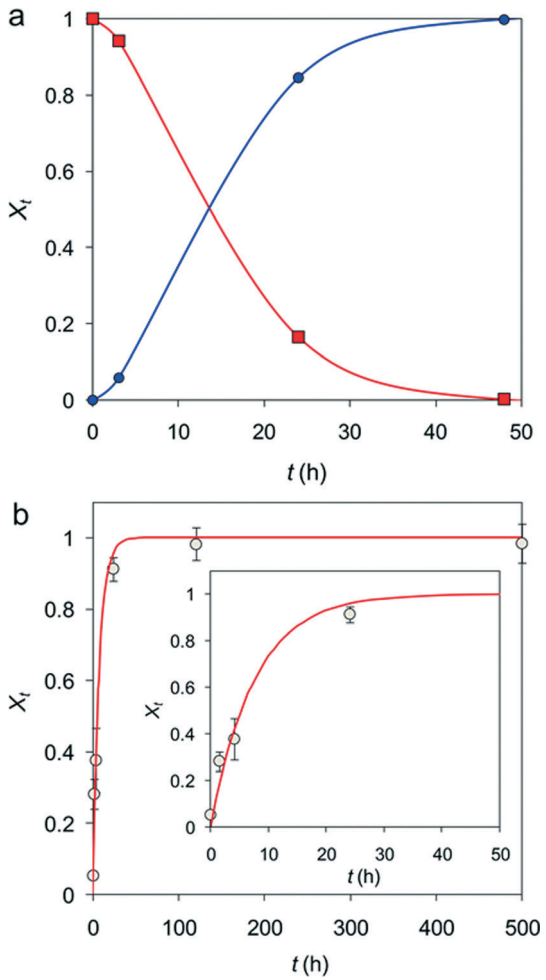

Fig. 11 Kinetics of nanolime carbonation. a) *t*-dependent conversion of portlandite into crystalline $CaCO_3$ determined using XRD results. Note that the conversion follows a S-shaped Avrami–Erofeev kinetic model. Legend: portlandite, red symbols and solid line; $CaCO_3$, blue symbols and solid line; b) experimental (circles) and calculated (model fitting to a deceleratory F1 kinetic model; solid red curve) results for the carbonation of nanolime considering the full amount of calcium carbonate (amorphous and crystalline) determined using TG. The inset shows details of the early stages of conversion.

for $t = 0$ to $t = t$ and $X_t = 0$ to $X_t = X_{max}$ (note that $X_{max} = 1$, if full conversion is achieved) yields

$$X_t = X_{max}(1 - \exp(-kt)) \quad (2)$$

Fig. 11b shows the fitting of the experimental data to the F1 kinetic model. Note that in eqn (2), k has no physical meaning. Therefore, we calculated $t_{1/2}$, the "half-carbonation time" (*i.e.* the time it takes to achieve a fractional conversion of 0.5), which is given by[18]

$$t_{1/2} = \frac{1}{kX_{max}} \quad (3)$$

and used this value to calculate the initial carbonation rate, v_0, by using the following equation:

$$v_0 = \frac{X_{max}}{t_{1/2}} = k(X_{max})^2 \quad (4)$$

v_0 is equal to 2.19×10^{-3} min^{-1}, a relatively high value which indicates that carbonation of nanolime in humid air at room *T* is a fast process, much faster (and with a higher yield) than the carbonation of standard slaked lime.[7] Finally, the overall good fitting with the deceleratory first-order kinetic model suggests that the carbonation of $Ca(OH)_2$ is controlled by the *t*-evolution of reactant concentration.[64]

3.6. Kinetics of vaterite and aragonite conversion into calcite

Fig. 12 shows the *t*-dependent variation of fractional vaterite and aragonite content (calculated from XRD results) during the progress of the carbonation of nanolime. Polymorph conversion displayed X_t–*t* deceleratory kinetics. We fitted the experimental data to the different deceleratory kinetic models indicated above. The best fitting was achieved using the F1 kinetic model (eqn (2)) for both vaterite (R^2 = 0.998) and aragonite (R^2 = 0.96). The corresponding v_0 values were 1.4×10^{-4} min^{-1} and 1.1×10^{-4} min^{-1}, respectively. Note that while in the case of aragonite a nearly full conversion (within error) was achieved after 21 days, in the case of vaterite, the experimental X_t after 21 days was only 0.72. The latter shows that a minor amount of vaterite will remain untransformed for (several) months after carbonation of nanolime is completed. Indeed, XRD analysis of nanolime samples exposed to atmospheric CO_2 at 80% RH for more than 5 months showed that they still included a minor (~5 wt%) amount of vaterite.

Considering that vaterite formation after nanolime application to porous stone results in a lower consolidation capacity than that achieved by the formation of calcite,[7] our kinetic results for the vaterite-to-calcite conversion indicate that the full performance of nanolimes as consolidants cannot be achieved within the first few weeks after application. Due to its minor

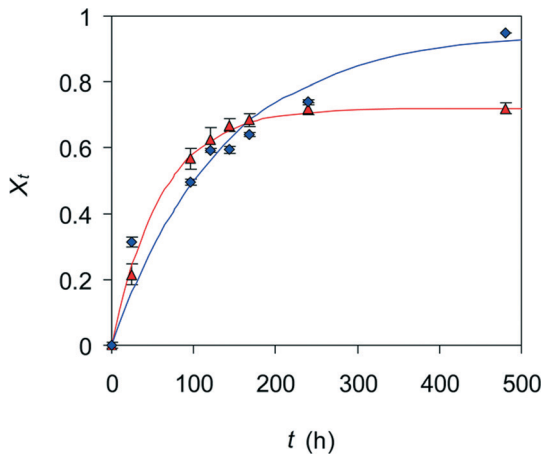

Fig. 12 Kinetics of vaterite and aragonite conversion into calcite. Experimental results (symbols) and fitting (solid lines) to a deceleratory first-order kinetic model for vaterite-to-calcite conversion (red triangles/line) and aragonite-to-calcite conversion (blue rhombs/line).

content, the detrimental effect of vaterite presence should, however, be negligible after *ca.* 10 days carbonation time (when ~0.7 fractional conversion into calcite is achieved).

Our kinetic results are in stark contrast to those reported for the vaterite-to-calcite conversion in solution. Linear (high supersaturation) or power-law (moderate supersaturation) kinetics have been typically observed and interpreted considering that the process involved the dissolution of vaterite and the subsequent nucleation and growth of calcite, the latter being the rate controlling step.[23,54,55] In contrast, our kinetic model suggests that in humid air the rate controlling step is not the growth of the product phase but the *t*-evolution of reactant (vaterite) concentration and, thus, its availability for dissolution. This also holds true for the aragonite-to-calcite conversion. Note that such a latter phase transformation reportedly occurs *via* a dissolution–precipitation mechanism (at low *T*),[41] possibly facilitated by high-defect densities.[65]

4. Conclusions

The carbonation of nanolime in humid air at room *T*, conditions that are typically found during field application of such a conservation material, involves classical and non-classical crystallization pathways. First, abundant (up to 24 wt%) ACC forms *via* an interface-coupled dissolution–precipitation mechanism that results in partially dissolved (with hollow faces) pseudomorphs after hexagonal plate-like portlandite. ACC also forms *via* homogeneous nucleation, thereby appearing as spherical nanoparticles. Subsequently, crystalline $CaCO_3$ polymorphs, vaterite (up to 35 wt%), minor aragonite (up to 5 wt%) and abundant calcite (which at the end of the carbonation process represents >95 wt%) form after dissolution of ACC. The solubility of ACC marks the supersaturation of the solution with respect to the crystalline polymorphs. Over time (after 24 h carbonation time), the metastable $CaCO_3$ polymorphs vaterite and aragonite start to transform into stable calcite *via* a dissolution–precipitation mechanism. Overall, the carbonation process follows the Ostwald's step rule, represented here by the sequence: ACC → vaterite → aragonite → calcite. Quantitatively, the process can be fitted to a deceleratory first-order kinetic model for both portlandite carbonation and vaterite-to-calcite and aragonite-to-calcite transformations. These kinetic results indicate that the rate limiting step during nanolime carbonation in humid air at room *T* is the amount of available unreacted $Ca(OH)_2$.

The growth of vaterite structures after ACC takes place *via* a non-classical nanoparticle-mediated process, where building units (primary vaterite nanoparticles), presumably formed *via* heterogeneous nucleation onto ACC, aggregate by mesoscale assembly into (nearly) iso-oriented structures (that resemble mesocrystals). Subsequently, vaterite structures dissolve and calcite crystals precipitate.

Aragonite spindle-like structures also form *via* self-assembly of primary rod-like nanoparticles, presumably formed following heterogeneous nucleation onto ACC. Over time, these structures either dissolve and transform into calcite or undergo Ostwald ripening, thereby resulting in large but scarce (not detected by XRD but observed using TEM and FESEM) aragonite prisms (with {110} twinning).

Calcite, the stable $CaCO_3$ polymorph (under STP conditions), is the main phase formed after nanolime carbonation. Its formation follows direct and indirect pathways. It can directly nucleate in solution and subsequently grow after dissolution of ACC and/or vaterite (and aragonite), or it may nucleate on vaterite (or aragonite) and, after such a heterogeneous nucleation, grow either *via* a non-classical particle-mediated (aggregation) mechanism or *via* a classical ion-mediated mechanism.

We unambiguously show that the formation of metastable vaterite and aragonite is directly related to the presence of ethanol adsorbed on portlandite nanoparticles: in its absence, only calcite is formed.

The fast kinetics of nanolime carbonation should ensure a rapid (within days) consolidation effect once this conservation material is applied on heritage structures or artworks. However, it is noted that the formation of metastable phases, particularly vaterite, may represent a handicap for the full short-term performance of nanolimes as a consolidant. In any case, the fast kinetics of the vaterite-to-calcite transformation (*i.e.* 0.72 fractional conversion within ten days) ensure that the almost full consolidation potential of nanolimes can be reached within weeks.

Finally, the remarkable mechanistic and kinetic similarities between nanolime carbonation in the presence of alcohol (which can be considered as an organic additive) and biomineralization/biomimetic synthesis of $CaCO_3$ underline that the observed multistep crystallization and non-classical crystal growth processes might be general and applicable for the rational design and application of novel $CaCO_3$ materials based, for instance, on routes involving nanolime precursors.

Acknowledgements

This work was financially supported by the Spanish Government (Grants CGL2012-35992 and CGL2015-70642-R), the Junta de Andalucía (Research Group RNM-179 and Project P11-RNM-7550), the Czech Grant Agency (GA ČR grant 14-20374P) and project No. LO1219 under the Ministry of Education, Youth and Sports National sustainability program I of Czech Republic. We thank the Centro de Instrumentación Científica (CIC, University of Granada) for analytical assistance and Dr. Alberto Viani and Petra Mácová (MSc) for QPA analysis and micro-Raman measurements, respectively.

References

1 E. Doehne and C. Price, *Stone Conservation: An Overview of Current Research*, 2nd edn, The Getty Conservation Institute, Los Angeles, 2010.
2 R. Giorgi, M. Baglioni, D. Berti and P. Baglioni, *Acc. Chem. Res.*, 2010, **43**, 695–704.

3 P. Baglioni, D. Chelazzi and R. Giorgi, *Nanotechnologies in the Conservation of Cultural Heritage*, Springer, New York, 2015.
4 D. Chelazzi, G. Poggi, Y. Jaidar, N. Toccafondi, R. Giorgi and P. Baglioni, *J. Colloid Interface Sci.*, 2013, **392**, 42–49.
5 G. M. Bond, J. Stringer, D. K. Brandvold, F. A. Simsek, M.-G. Medina and G. Egeland, *Energy Fuels*, 2001, **15**, 309–316.
6 O. Cizer, C. Rodriguez-Navarro, E. Ruiz-Agudo, J. Elsen, D. Van Gemert and K. Van Balen, *J. Mater. Sci.*, 2012, **47**, 6151–6165.
7 C. Rodriguez-Navarro, A. Suzuki and E. Ruiz-Agudo, *Langmuir*, 2013, **29**, 11457–11470.
8 M. Drdácký, Z. Slížková and G. Ziegenbalg, *J. Nanopart. Res.*, 2008, **8**, 13–22.
9 P. Baglioni, D. Chelazzi, R. Giorgi, E. Carretti, N. Toccafondi and Y. Jaidar, *Appl. Phys. A: Mater. Sci. Process.*, 2014, **114**, 723–732.
10 P. Lopez-Arce, L. S. Gómez-Villalba, S. Martínez-Ramírez, M. Álvarez de Buergo and R. Fort, *Powder Technol.*, 2011, **205**, 263–269.
11 L. S. Gomez-Villalba, P. López-Arce, M. Álvarez de Buergo and R. Fort, *Appl. Phys. A: Mater. Sci. Process.*, 2011, **104**, 1249–1254.
12 L. S. Gomez-Villalba, P. López-Arce, M. Álvarez de Buergo and R. Fort, *Appl. Phys. A: Mater. Sci. Process.*, 2012, **106**, 213–217.
13 T. Ogino, T. Suzuki and K. Sawada, *Geochim. Cosmochim. Acta*, 1987, **51**, 2757–2767.
14 F. Meldrum and H. Cölfen, *Chem. Rev.*, 2008, **108**, 4332–4432.
15 M. H. Nielsen, S. Aloni and J. J. De Yoreo, *Science*, 2014, **345**, 1158–1162.
16 H. Yagi, A. Iwazawa, R. Sonobe, T. Matsubara and H. Hikita, *Ind. Eng. Chem. Res.*, 1984, **23**, 153–158.
17 J. García-Carmona, J. Gómez-Morales and R. Rodríguez-Clemente, *J. Cryst. Growth*, 2003, **249**, 561–571.
18 G. Montes-Hernandez, F. Renard, N. Geoffroy, L. Charlet and J. Pironon, *J. Cryst. Growth*, 2007, **308**, 228–236.
19 G. Montes-Hernandez, A. Pommerol, F. Renard, P. Beck, E. Quirico and O. Brissaud, *Chem. Eng. J.*, 2010, **161**, 250–256.
20 C. Rodriguez-Navarro, K. Kudlacz, Ö. Cizer and E. Ruiz-Agudo, *CrystEngComm*, 2015, **17**, 58–72.
21 J. R. Clarkson, T. J. Price and C. J. Adams, *J. Chem. Soc., Faraday Trans.*, 1992, **88**, 243–249.
22 C. Tai and F.-B. Chen, *AIChE J.*, 1998, **44**, 1790–1798.
23 J. D. Rodriguez-Blanco, S. Shaw and L. G. Benning, *Nanoscale*, 2011, **3**, 265–271.
24 K. Van Balen, *Cem. Concr. Res.*, 2005, **35**, 647–657.
25 E. Ruiz-Agudo, K. Kudłacz, C. V. Putnis, A. Putnis and C. Rodriguez-Navarro, *Environ. Sci. Technol.*, 2013, **47**, 11342–11349.
26 S.-M. Shih, C.-S. Ho, Y.-S. Song and J.-P. Lin, *Ind. Eng. Chem. Res.*, 1999, **38**, 1316–1322.
27 D. T. Beruto and R. Botter, *J. Eur. Ceram. Soc.*, 2000, **20**, 497–503.
28 R. M. Dheilly, J. Tudo, Y. Sebaïbi and M. Quéneudec, *Constr. Build. Mater.*, 2002, **16**, 155–161.
29 T. Yang, B. Keller, E. Gagyari, K. Hametner and D. Günther, *J. Mater. Sci.*, 2003, **38**, 1909–1916.
30 W.-S. Kim, I. Hirasawa and W.-S. Kim, *Ind. Eng. Chem. Res.*, 2004, **43**, 2650–2657.
31 H. M. Rietveld, *J. Appl. Crystallogr.*, 1969, **2**, 65–71.
32 N. Koga and Y. Yamane, *J. Therm. Anal. Calorim.*, 2008, **94**, 379–387.
33 A. Putnis, *Rev. Mineral. Geochem.*, 2009, **70**, 87–124.
34 S. Kamhi, *Acta Crystallogr.*, 1963, **16**, 770–772.
35 H. J. Meyer, *Z. Kristallogr., Kristallgeom., Kristallphys., Kristallchem.*, 1969, **128**, 183–212.
36 R. Demichelis, P. Raiteri, J. D. Gale and R. Dovesi, *Cryst. Growth Des.*, 2013, **13**, 2247–2251.
37 R. Ševčík, M. Pérez-Estébanez, A. Viani, P. Šašek and P. Mácová, *Powder Technol.*, 2015, **284**, 265–271.
38 L. Kabalah-Amitai, B. Mayzel, Y. Kauffmann, A. N. Fitch, L. Bloch, P. U. P. A. Gilbert and B. Pokroy, *Science*, 2013, **340**, 454–457.
39 P. Bots, L. G. Benning, J. D. Rodriguez-Blanco, T. Roncal-Herrero and S. Shaw, *Cryst. Growth Des.*, 2012, **12**, 3806–3814.
40 Q. Shen, H. Wei, Y. Zhou, Y. Huang, H. Yang, D. Wang and D. Xu, *J. Phys. Chem. B*, 2006, **110**, 2994–3000.
41 K. K. Sand, J. D. Rodriguez-Blanco, E. Makovicky, L. G. Benning and S. L. S. Stipp, *Cryst. Growth Des.*, 2012, **12**, 842–853.
42 S. F. Chen, S. H. Yu, J. Jiang, F. Li and Y. Liu, *Chem. Mater.*, 2006, **18**, 115–122.
43 H. Cölfen and M. Antonietti, *Mesocrystals and Noncalssical Crystallization*, Wiley, Weinheim, 2008.
44 R. Q. Song, H. Cölfen, A. W. Xu, J. Hartmann and M. Antonietti, *ACS Nano*, 2009, **3**, 1966–1978.
45 N. Gehrke, H. Cölfen, N. Pinna, M. Antonietti and N. Nassif, *Cryst. Growth Des.*, 2005, **5**, 1317–1319.
46 Y. Zhu, Y. Liu, Y. Ruan, J. Xiao, Z. Liu, L. Cheng, F. Xu and L. Zhang, *J. Phys. Chem. C*, 2009, **113**, 6584–6588.
47 J. J. De Yoreo, P. U. P. A. Gilbert, N. A. J. M. Sommerdijk, R. L. Penn, S. Whitelam, D. Joester, H. Zhang, J. D. Rimer, A. Navrotsky, J. F. Banfield, A. F. Wallace, F. M. Michel, F. C. Meldrum, H. Cölfen and P. M. Dove, *Science*, 2015, **349**, 498.
48 J.-P. Andreassen, *J. Cryst. Growth*, 2005, **274**, 256–264.
49 G.-T. Zhou, Q.-Z. Yao, J. Ni and G. Jin, *Am. Mineral.*, 2009, **94**, 293–302.
50 Y. Oaki and H. Imai, *Small*, 2006, **2**, 66–70.
51 J. Seto, Y. Ma, S. A. Davis, F. Meldrum, A. Gourrier, Y.-Y. Kim, U. Schilde, M. Sztucki, M. Burghammer, S. Maltsev, C. Jäger and H. Cölfen, *Proc. Natl. Acad. Sci. U. S. A.*, 2012, **109**, 3699–3704.
52 Y.-Y. Kim, A. S. Schenk, J. Ihli, A. N. Kulak, N. B. J. Hetherington, C. C. Tang, W. W. Schmahl, E. Griesshaber, G. Hyett and F. C. Meldrum, *Nat. Commun.*, 2014, **5**, 4341.
53 C. Rodriguez-Navarro, A. Burgos Cara, K. Elert, C. V. Putnis and E. Ruiz-Agudo, *Cryst. Growth Des.*, 2016, **16**, 1850–1860.
54 T. Ogino, T. Suzuki and K. Sawada, *J. Cryst. Growth*, 1990, **100**, 159–167.

55 N. Spanos and P. G. Koutsoukos, *J. Cryst. Growth*, 1998, **191**, 783–790.
56 C. Rodriguez-Navarro, I. Vettori and E. Ruiz-Agudo, *Langmuir*, 2016, **32**, 5183–5194.
57 U. Wehrmeister, D. E. Jacob, A. L. Soldati, N. Loges, T. Hager and W. Hofmeister, *J. Raman Sspectrosc.*, 2011, **42**, 926–935.
58 S. R. Dickinson and K. M. McGrath, *J. Mater. Chem.*, 2003, **13**, 928–933.
59 K.-S. Seo, C. Han, J.-H. Wee, J.-K. Park and J.-W. Ahn, *J. Cryst. Growth*, 2005, **276**, 680–687.
60 L. Zhang, L.-H. Yue, F. Wang and Q. Wang, *J. Phys. Chem. B*, 2008, **112**, 10668–10674.
61 F. Manoli and E. Dalas, *J. Cryst. Growth*, 2000, **218**, 359–364.
62 K. K. Sand, M. Yang, E. Makovicky, D. J. Cooke, T. Hassenkam, K. Bechgaard and S. L. S. Stipp, *Langmuir*, 2010, **26**, 15239–15247.
63 K. S. Keller, M. H. M. Olsson, M. Yang and S. L. S. Stipp, *Langmuir*, 2015, **31**, 3847–3853.
64 A. Khawan and D. R. Flanagan, *J. Phys. Chem. B*, 2006, **110**, 17315–17328.
65 L. S. Gomez-Villalba, P. López-Arce, M. Alvarez de Buergo and R. Fort, *Cryst. Growth Des.*, 2012, **12**, 4844–4852.